

A staggered-grid finite-difference method with perfectly matched layers for poroelastic wave equations

Yan Qing Zeng and Qing Huo Liu^{a)}

Department of Electrical and Computer Engineering, Duke University, Durham, North Carolina 27708

(Received 1 November 2000; accepted for publication 3 March 2001)

A particle velocity-strain, finite-difference (FD) method with a perfectly matched layer (PML) absorbing boundary condition is developed for the simulation of elastic wave propagation in multidimensional heterogeneous poroelastic media. Instead of the widely used second-order differential equations, a first-order hyperbolic leap-frog system is obtained from Biot's equations. To achieve a high accuracy, the first-order hyperbolic system is discretized on a staggered grid both in time and space. The perfectly matched layer is used at the computational edge to absorb the outgoing waves. The performance of the PML is investigated by calculating the reflection from the boundary. The numerical method is validated by analytical solutions. This FD algorithm is used to study the interaction of elastic waves with a buried land mine. Three cases are simulated for a mine-like object buried in "sand," in purely dry "sand" and in "mud." The results show that the wave responses are significantly different in these cases. The target can be detected by using acoustic measurements after processing. © 2001 Acoustical Society of America.

[DOI: 10.1121/1.1369783]

PACS numbers: 43.20.Bi, 43.20.Fn, 43.20.Gp [ANN]

I. INTRODUCTION

Simulation of elastic waves propagating in fluid-saturated porous media is of great importance to geophysical exploration, reservoir engineering, and military applications.

With the increasing difficulty of exploring natural resources and the growing realization that hydrocarbon reservoirs are more heterogeneous and complex than assumed in the past, it is desirable to characterize the subsurface materials as fluid-saturated porous media than perfectly elastic single phase materials.

In military applications, simulation of waves in porous media is important for underwater acoustics. More recently, acoustic waves are used for land mine detection. For plastic land mines, acoustic waves provide a much better measurement than the traditional electromagnetic induction method. Although the soil can be approximated as a single phase elastic material, it is more accurate to treat soil as two phase composite materials consisting of granular solid and pore fluid.

Simulation of wave propagation in porous, fluid-saturated media requires the analytical or numerical solution of Biot's equations.¹⁻³ For a heterogeneous, complex model, in general it is not possible to find analytical solutions to Biot's equations. Numerical methods have to be used to obtain these solutions. Finite-difference (FD) algorithms have been developed to simulate wave propagation in poroacoustic media,⁴ and in homogeneous poroelastic media.⁵ A centered-grid FD scheme has also been developed for heterogeneous poroelastic media.⁶ In this article, a velocity-strain, finite-difference method is developed in a staggered grid for heterogeneous poroelastic media. In this method, Biot's equations³ are reformulated into first-order equations to ar-

rive at a leap-frog system in a staggered grid both in time and space domains. Numerical solutions have been validated by analytical solutions.

In order to simulate an unbounded medium, an absorbing boundary condition (ABC) must be implemented to truncate the computational domain in numerical algorithms. There are many kinds of ABCs developed for numerical simulation of wave propagation. Cerjan *et al.*⁷ introduced a simple damping taper to the boundaries to attenuate the outgoing waves. Since this lossy layer is not perfectly matched to the interior region, however, it requires a substantial number of layers for the taper to be effective. Clayton and Engquist⁸ (CE) use the paraxial approximation to the wave equation to make the boundary transparent to outgoing waves. The CE ABC can lead to instability when the Poisson ratio is greater than 2.⁹ Since Berenger¹⁰ proposed the highly effective perfectly matched layer (PML) as an absorbing boundary condition for electromagnetic waves, the PML has been widely used for finite-difference and finite-element methods. Chew and Liu^{11,12} first proposed the PML for elastic waves in solids, and proved the zero reflections from PML to the regular elastic medium. Hastings *et al.*¹³ have independently implemented the PML ABC for two-dimensional problems by using potentials. The PML has also been extended to model acoustic waves and electromagnetic waves in lossy media.¹⁴ The PML has been applied to the second-order Biot's equation for fluid-saturated poroelastic media,¹⁵ which requires a complicated convolution. In this article, as the PML is developed for the first-order system, incorporation of PML becomes much simpler. The effectiveness of this ABC is confirmed by examining the reflection from the boundary.

By using this numerical method, interaction of elastic waves with a buried plastic minelike object is investigated. Three cases are simulated for a plastic minelike object buried

^{a)}Electronic mail: qhliu@ee.duke.edu

in “sand,” in purely dry “sand” and in “mud.” The results show that the wave responses are significantly different in these cases. After processing, the target can be detected by using surface acoustic measurements.

II. FORMULATION

A. The governing equations

The propagation of acoustic waves in porous and fluid-saturated media is different from that in single phase elastic media. In addition to the regular P waves and S waves in solid elastic media, a slow P wave which results from the relative motion between solid frame and fluid may be present in porous media. Thus the pattern of energy dissipation in porous media is different from that in solid elastic media. Based on continuum mechanics and macroscopic constitutive relationship, Biot¹⁻³ developed a theory of wave motion in a porous elastic solid saturated with a viscous compressible fluid. Biot’s theory was confirmed by Burridge and Keller¹⁶ based on the dynamic equations which govern the behavior of medium on a microscopic scale. Plona¹⁷ also confirmed Biot’s theory through experiments.

In an isotropic, heterogeneous porous elastic medium, the parameters describing the physical properties of the medium are as follows:

μ	shear modulus of dry porous matrix
λ_c	Lame constant of saturated matrix
ϕ	porosity
η	viscosity
κ	permeability
ρ	the overall density of the saturated medium determined by $\rho_f\phi + (1 - \phi)\rho_s$
ρ_s	density of solid material
ρ_f	density of fluid
a	tortuosity of the matrix
K_s	bulk modulus of the solid
K_f	bulk modulus of the fluid
K_b	bulk modulus of the dry porous frame

The macroscopic displacements and strains are defined as

u_i	i th component of displacements of solid particle
U_i	i th component of displacements of fluid particle
w_i	i th component of relative displacement, $w_i = \phi(U_i - u_i)$
e_{il}	il component of strain tensor in porous medium, $e_{il} = [((\partial u_i / \partial x_j) + (\partial u_j / \partial x_i)) / 2]$
e	$e = \sum_{i=1,2,3} e_{ii}$
ξ	dilatation for the relative motion, $\xi = -\sum_{i=1,2,3} (\partial w_i / x_i)$

For a three-dimensional isotropic, heterogeneous and porous elastic medium, wave propagation is governed by Biot’s equations:³

$$2 \sum_l \frac{\partial}{\partial x_l} (\mu e_{il}) + \frac{\partial}{\partial x_i} (\lambda_c e - \alpha M \xi) = \frac{\partial^2}{\partial t^2} (\rho u_i + \rho_f w_i), \quad (1)$$

$$\frac{\partial}{\partial x_i} (\alpha M e - M \xi) = \frac{\partial^2}{\partial t^2} (\rho_f u_i + m w_i) + \frac{\eta}{\kappa} \frac{\partial w_i}{\partial t}, \quad (2)$$

where $m = a \rho_f / \phi$ and

$$M = \frac{1}{\phi / K_f + (\alpha - \phi) / K_s}, \quad \alpha = 1 - \frac{K_b}{K_s}.$$

Let \mathbf{v}^s be the velocity of the solid particle, and \mathbf{v}^f be the velocity of the pore fluid relative to the solid frame. Then the second-order equations (1) and (2) can be rearranged as the first-order equations

$$(m\rho - \rho_f^2) \frac{\partial v_i^s}{\partial t} = 2m \sum_l \frac{\partial}{\partial x_l} (\mu e_{il}) + m \frac{\partial}{\partial x_i} (\lambda_c e - \alpha M \xi) - \rho_f \frac{\partial}{\partial x_i} (\alpha M e - M \xi) + \rho_f \frac{\eta}{\kappa} v_i^f, \quad (3)$$

$$(m\rho - \rho_f^2) \frac{\partial v_i^f}{\partial t} = \rho \frac{\partial}{\partial x_i} (\alpha M e - M \xi) - \rho \frac{\eta}{\kappa} v_i^f - 2\rho_f \sum_l \frac{\partial}{\partial x_l} (\mu e_{il}) - \rho_f \frac{\partial}{\partial x_i} (\lambda_c e - \alpha M \xi). \quad (4)$$

The time derivatives of strains e_{il} and ξ can be expressed as

$$\frac{\partial e_{il}}{\partial t} = [(\partial v_i^s / \partial x_l + \partial v_l^s / \partial x_i) / 2], \quad (5)$$

$$\frac{\partial \xi}{\partial t} = -\nabla \cdot \mathbf{v}^f. \quad (6)$$

In the explicit first-order finite-difference schemes, Eqs. (3)–(6) consist of a leap-frog system for the strain field e_{il} , ξ and velocity field \mathbf{v}^s and \mathbf{v}^f . With proper absorbing boundary conditions, these equations can be solved numerically for the wave field in an unbounded medium.

Equations (3)–(6) predict the existence of three different waves in fluid-saturated poroelastic media: a shear wave and two compressional waves with a faster and a slower propagation velocities.

B. Equations for the PML absorbing boundary condition

In this article, the perfectly matched layer (PML) will be used to truncate the unbounded medium, absorbing all outgoing waves. The artificial absorptive medium is introduced in the regular medium by modifying Eqs. (3)–(6) with complex coordinates.^{12,13,15} In the frequency domain (where a time-harmonic factor $e^{-j\omega t}$ is implied and $j = \sqrt{-1}$), a complex coordinate variable is chosen as

$$\tilde{x}_i = \int_0^{x_i} e_i(x'_i) dx'_i, \quad (7)$$

$$e_i = a_i + j \frac{\omega_i}{\omega} \quad (i = 1, 2, 3), \quad (8)$$

where $a_i \geq 1$ is a scaling factor, and $\omega_i \geq 0$ is an attenuation factor. The operator $\partial/\partial x_i$ can be expressed in terms of the regular coordinate,

$$\frac{\partial}{\partial \tilde{x}_i} = \frac{1}{e_i} \frac{\partial}{\partial x_i}. \quad (9)$$

The PML formulation is to replace x_i in (3)–(6) by the corresponding complex coordinate \tilde{x}_i . In a PML region, the real part a_i is a scaling factor, and the imaginary part ω_i represents a loss in the PML. In a regular non-PML region, $a_i = 1$ and $\omega_i = 0$.

In order to simplify the PML equations, the field variables are split as follows:

$$v_i^s = \sum_{k=1}^3 v_i^{s(k)}, \quad v_i^f = \sum_{k=1}^3 v_i^{f(k)},$$

where $v_i^{s(k)}$ and $v_i^{f(k)}$ represent the split field variables containing space derivative $\partial/\partial x_k$ only. For example, Eq. (3) for $i=1$ can be split into the following three equations,

$$(m\rho - \rho_f^2) \frac{\partial v_1^{s(1)}}{\partial t} = 2m \frac{\partial}{\partial x_1} (\mu e_{11}) + m \frac{\partial}{\partial x_1} (\lambda_c e - \alpha M \xi) - \rho_f \frac{\partial}{\partial x_1} (\alpha M e - M \xi),$$

$$(m\rho - \rho_f^2) \frac{\partial v_1^{s(2)}}{\partial t} = 2m \frac{\partial}{\partial x_2} (\mu e_{12}) + \rho_f \frac{\eta}{\kappa} v_1^f,$$

$$(m\rho - \rho_f^2) \frac{\partial v_1^{s(3)}}{\partial t} = 2m \frac{\partial}{\partial x_3} (\mu e_{13}).$$

The diagonal strain components e_{ii} need not be split. However, other strain components have to be split as $e_{il} = \sum_{k=1}^3 e_{il}^{(k)}$ for $i \neq l$, and $\xi = \sum_{k=1}^3 \xi^{(k)}$. For example, from (5) we have

$$\frac{\partial e_{ii}}{\partial t} = \frac{\partial v_i^s}{\partial x_i},$$

$$e_{12} = e_{12}^{(1)} + e_{12}^{(2)},$$

$$\frac{\partial e_{12}^{(1)}}{\partial t} = \frac{1}{2} \frac{\partial v_2^s}{\partial x_1}, \quad \frac{\partial e_{12}^{(2)}}{\partial t} = \frac{1}{2} \frac{\partial v_1^s}{\partial x_2},$$

$$\xi = \xi^{(1)} + \xi^{(2)} + \xi^{(3)},$$

$$\frac{\partial \xi^{(1)}}{\partial t} = -\frac{\partial v_1^f}{\partial x_1},$$

$$\frac{\partial \xi^{(2)}}{\partial t} = -\frac{\partial v_2^f}{\partial x_2}, \quad \frac{\partial \xi^{(3)}}{\partial t} = -\frac{\partial v_3^f}{\partial x_3}.$$

In frequency domain PML formulation, after x_i is replaced by \tilde{x}_i , equations for v_1^s , for example, can be rewritten as

$$(m\rho - \rho_f^2)(-j\omega) \left(1 + j \frac{\omega_{x_1}}{\omega} \right) v_1^{s(1)} = 2m \frac{\partial}{\partial x_1} (\mu e_{11}) + m \frac{\partial}{\partial x_1} (\lambda_c e - \alpha M \xi) - \rho_f \frac{\partial}{\partial x_1} (\alpha M e - M \xi),$$

$$(m\rho - \rho_f^2)(-j\omega) \left(1 + j \frac{\omega_{x_1}}{\omega} \right) v_1^{s(2)} = 2m \frac{\partial}{\partial x_2} (\mu e_{12}) + \left(1 + j \frac{\omega_1}{\omega} \right) \rho_f \frac{\eta}{\kappa} v_1^f,$$

$$(m\rho - \rho_f^2)(-j\omega) \left(1 + j \frac{\omega_1}{\omega} \right) v_1^{s(3)} = 2m \frac{\partial}{\partial x_3} (\mu e_{13}).$$

By taking the inverse Fourier transform, the above equations yield the time-domain PML equations,

$$(m\rho - \rho_f^2) \left(\frac{\partial v_1^{s(1)}}{\partial t} + \omega_1 v_1^{s(1)} \right) = 2m \frac{\partial}{\partial x_1} (\mu e_{11}) + m \frac{\partial}{\partial x_1} (\lambda_c e - \alpha M \xi) - \rho_f \frac{\partial}{\partial x_1} (\alpha M e - M \xi), \quad (10)$$

$$(m\rho - \rho_f^2) \left(\frac{\partial v_1^{s(2)}}{\partial t} + \omega_1 v_1^{s(2)} \right) = 2m \frac{\partial}{\partial x_2} (\mu e_{12}) + \rho_f \frac{\eta}{\kappa} \left(v_1^f + \omega_2 \int_{-\infty}^t v_1^f d\tau \right), \quad (11)$$

$$(m\rho - \rho_f^2) \left(\frac{\partial v_1^{s(3)}}{\partial t} + \omega_1 v_1^{s(3)} \right) = 2m \frac{\partial}{\partial x_3} (\mu e_{13}), \quad (12)$$

$$\frac{\partial e_{11}}{\partial t} = \frac{\partial v_1}{\partial x_1} - \omega_1 e_{11}, \quad (13)$$

$$\frac{\partial e_{12}^{(1)}}{\partial t} = \frac{1}{2} \frac{\partial v_2^s}{\partial x_1} - \omega_1 e_{12}^{(1)}, \quad (14)$$

$$\frac{\partial e_{12}^{(2)}}{\partial t} = \frac{1}{2} \frac{\partial v_1^s}{\partial x_2} - \omega_2 e_{12}^{(2)}, \quad (15)$$

$$\frac{\partial \xi^{(1)}}{\partial t} = -\frac{\partial v_1^f}{\partial x_1} - \omega_1 \xi^{(1)}, \quad (16)$$

$$\frac{\partial \xi^{(2)}}{\partial t} = -\frac{\partial v_2^f}{\partial x_2} - \omega_2 \xi^{(2)}, \quad (17)$$

$$\frac{\partial \xi^{(3)}}{\partial t} = -\frac{\partial v_3^f}{\partial x_3} - \omega_3 \xi^{(3)}. \quad (18)$$

Similar equations can be obtained in the same way for other components v_2^s , v_3^s , v_1^f , v_2^f , v_3^f , and e_{13} , e_{23} . Within the PML region, Eqs. (3) and (4) are split into 18 equations for 3D. Equation (5) is split into nine equations and Eq. (6) is split into three equations. So the total number of the equa-

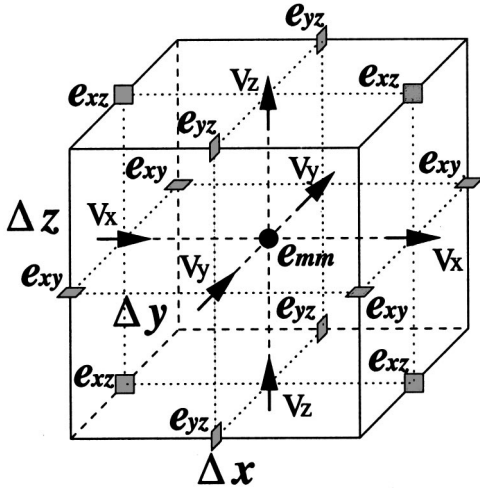


FIG. 1. The relative locations of field components in a unit cell of staggered grid.

tions is 30 for the PML region, compared to 13 for the regular interior region. Thus, the memory requirement within the PML region is about two and half times that required by a regular medium for three-dimensional problems. This extra memory requirement in the PML region is offset by the effectiveness of PML in absorbing the outgoing waves.

C. Finite-difference implementation

The governing equations for the PML absorbing boundary condition, such as Eqs. (10)–(18), are first-order partial differential equations for particle velocity and strain. They can be solved with different numerical methods. For the evaluation of seismic and acoustic responses of specific models, the accuracy and convenience of the numerical method are of primary concern. The finite-difference method is widely used in wave modeling because of its flexibility and accuracy. For the first-order, leap-frog system of Eqs. (3)–(6) and (10)–(18), the explicit finite-difference method is used on a staggered grid.

To implement a 3-D finite-difference solution to the equations with the PML, the material parameters and unknown field components are discretized on a regular 3-D grid at the intervals Δx_1 , Δx_2 and Δx_3 . The time domain is also discretized with time step Δt . There are two discretization schemes to approximate the first-order derivatives, i.e., the centered grid and the staggered grid. Because the centered-grid operator to perform first derivatives is less accurate than the staggered grid operator,¹⁸ a staggered grid is used in this article. For the FD implementation of Biot's equations on a staggered grid in Fig. 1, the velocity field components are located at the cell's face centers, while material parameters and normal strains are located at the center of the cell, and shear strains are located the at six edge centers. Strain field is computed at $n\Delta t$ and velocity field is computed at $(n + \frac{1}{2})\Delta t$. This staggered grid is similar to that for elastic waves in a solid.^{19,20}

With this discretization, the leap-frog system can be written in a time-stepping form. In order to make the layout of the formulas simple, the governing equations with PML

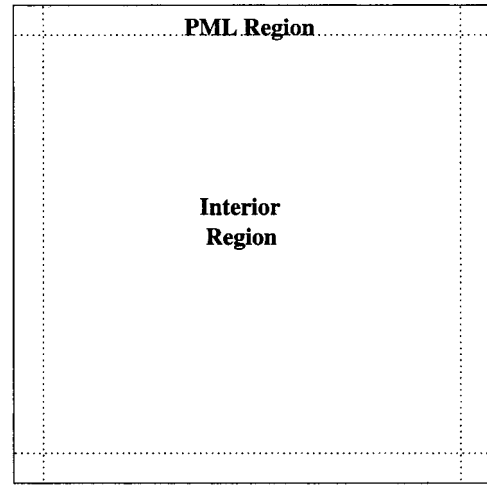


FIG. 2. Computational domain with an interior region and a PML boundary region.

boundary conditions can be generalized as the first-order differential equation. For examples, (11), (13) and (16) can be rewritten as

$$\frac{\partial v_1^{s(2)}}{\partial t} + c_0 v_1^{s(2)} = c_1 \int_{-\infty}^t v_1^f d\tau + c_2 \left[2m \frac{\partial}{\partial x_2} (\mu e_{12}) + \rho_f \frac{\eta}{\kappa} (v_1^f) \right], \quad (19)$$

$$\frac{\partial e_{11}}{\partial t} + \omega_1 e_{11} = \frac{\partial v_2^s}{\partial x_1}, \quad (20)$$

$$\frac{\partial \xi^{(1)}}{\partial t} + \omega_1 \xi^{(1)} = -\frac{\partial v_1^f}{\partial x_1}, \quad (21)$$

where c_0 , c_1 and c_2 space-dependent coefficients. The corresponding time-stepping equations can then be written as

$$v_1^{s(2)}[j_1, j_2, j_3, (n + \frac{1}{2})] = f_1 v_1^{s(2)}[j_1, j_2, j_3, (n - \frac{1}{2})] + f_2 R_1, \quad (22)$$

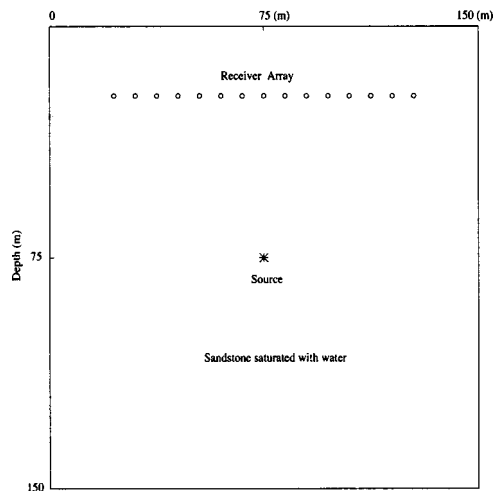


FIG. 3. A physical model showing source and receiver geometry used to generate seismograms. Receivers are 7.5 m apart.

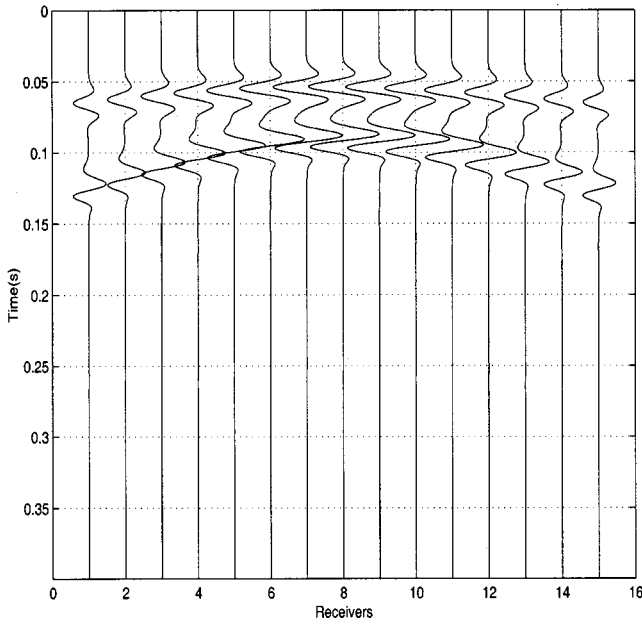


FIG. 4. Vertical velocity components waveforms of the model in Fig. 3.

$$e_{11}[j_1, j_2, j_3, (n+1)] = g_1 e_{11}[j_1, j_2, j_3, n] + g_2 R_2, \quad (23)$$

$$\xi^{(1)}[j_1, j_2, j_3, (n+1)] = -g_1 \xi^{(1)}[j_1, j_2, j_3, n] - g_2 R_3, \quad (24)$$

$$f_1 = \frac{c_0/2 - 1/\Delta t}{1/\Delta t + c_0/2}, \quad f_2 = \frac{1}{1/\Delta t + c_0/2},$$

$$g_1 = \frac{\omega_1/2 - 1/\Delta t}{1/\Delta t + \omega_1/2}, \quad g_2 = \frac{1}{1/\Delta t + \omega_1/2},$$

where R_1 , R_2 and R_3 are the right-hand sides of Eqs. (19), (20) and (21) respectively. It should be noted that the material parameters in the above equations must be properly averaged in order to arrive at a higher accuracy.¹⁹ In order to incorporate the PML boundary condition, the computational domain is divided into a PML region and an interior region, as shown in Fig. 2. The absorption of outgoing waves is achieved by the PML region, which consists of several cells of mathematically defined materials with a quadratically tapered ω_i profile to increase the attenuation toward the outer boundary. In this article, ω_i of the PML region is chosen as

$$\omega_i(j_i) = \frac{(M - 1/2 - j_i)^2}{(M - 1/2)^2} \omega_{i,\max}, \quad (25)$$

where $\omega_{i,\max}$ is the value at the center of the cell at the outermost boundary. At the outer boundary, the velocity components and shear strain are forced to be zero. For convenience, $\omega_{i,\max}$ can be expressed in terms of dominant frequency and a normalized coefficient a_0 . Then Eq. (25) becomes

$$\omega_i = \begin{cases} 2\pi a_0 f_0 (l_{x_i}/L_{\text{PML}})^2, & \text{inside PML,} \\ 0, & \text{outside PML,} \end{cases} \quad (26)$$

where f_0 is the dominant frequency of the source, L_{PML} is the thickness of the PML region, and l_{x_i} is the distance from the interface between the interior region and the PML region.

III. NUMERICAL RESULTS

The finite-difference algorithm on a staggered grid has a higher accuracy than on a centered grid. Thus, the PML region can be made thinner with a staggered grid with a better absorption than with a centered grid. In this article, the length of the PML region is chosen to be 10 cells. The FD algorithm is illustrated by its two-dimensional implementation.

In the following numerical results, a pure P-wave source is used to excite the seismic wave field. The source time function is the first derivative of a Gaussian function

$$S(t) = (t - t_0) e^{-\pi^2 f_0^2 (t - t_0)^2},$$

where f_0 is the predetermined dominant frequency, and t_0 the time shift.

Unless otherwise stated, a bulk source is used in the following examples. The source energy is partitioned linearly between the solid and the fluid phases with factors

$$W_f = \phi, \quad W_s = (1 - \phi), \quad W_r = \phi |W_f - W_s|,$$

where W_f is the weighting factor for the fluid motion, W_s is for the solid motion and W_r is for the relative motion between solid frame and pore fluid.

A. PML performance

The effectiveness of the absorbing boundary condition is an essential factor for the successful numerical simulation. A good absorbing boundary condition has the characteristics of effective absorption of outgoing waves without requiring a large memory. In this article, the performance of the PML is investigated on a homogeneous, fluid-saturated poroelastic

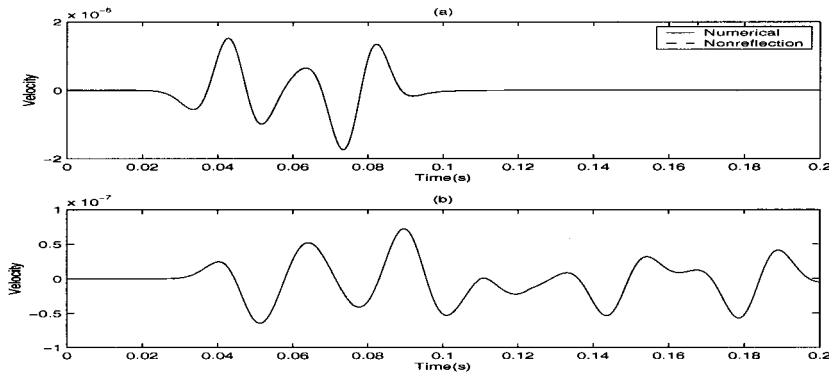


FIG. 5. (a) Comparison of numerical solution at a location 5 cells away from the PML boundary in the model in Fig. 3 with a reference solution. (b) The difference between these two solutions.

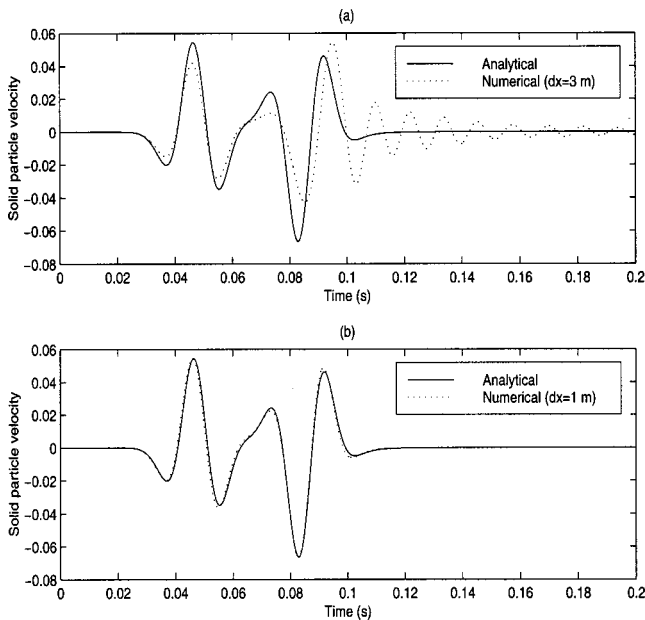


FIG. 6. Comparison of analytical and numerical solutions for the vertical velocity component in the solid for (a) $\Delta x=3$ m and (b) $\Delta x=1$ m.

medium by comparing numerical solutions of PML model with reference solutions that do not have reflections. The optimized a_0 can be obtained by examining the attenuation of the wave field in the PML region.

The homogeneous model for the PML performance test is a sandstone fully saturated with water having the properties of $\rho_s=2650$ kg/m³, $\rho_f=1040$ kg/m³, and porosity $\phi=0.3$. This model has the wave properties $v_{fast}=2365.7$ m/s for fast P wave, $v_{slow}=776.95$ m/s for slow P wave and $v_{shear}=960.5$ m/s for shear wave. The geometry of the physical model with receivers and source is shown in Fig. 3.

Figure 4 shows the numerical results of vertical velocity in solid from the model with the PML boundary condition. With the PML region, the reflections are eliminated from the seismograms. Another advantage of the PML absorbing boundary condition is its stability. For this particular model, $v_{fast}/v_{shear}=2.46$, which will cause an instability problem for the CE boundary condition.¹⁰

In order to quantify the reflections from the PML boundary, the reflection coefficient in dB is calculated for a location 5 cells away from PML interface in this model. The reflection was obtained by comparing the numerical results from the model with the PML boundary to those from a

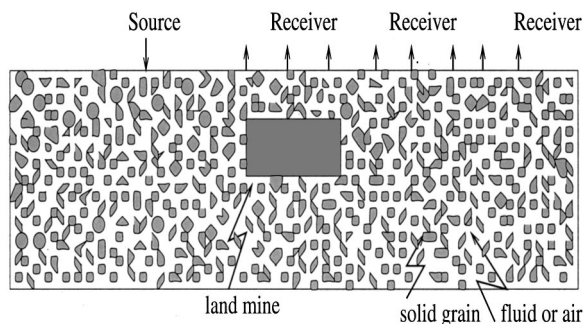


FIG. 7. Geometry of the model of a buried minelike object.

TABLE I. Properties of sand and mud (from Ref. 21).

	Sand	Mud
Porosity	0.4	0.6
Density (kg/m ³)	1990	1660
Structure factor	1.8	1.9
Permeability (m ²)	3×10^{-11}	3×10^{-13}
Bulk modulus (Pa)	4×10^7	1×10^7
Shear modulus (Pa)	2.2×10^7	6×10^6

much larger model with the Dirichlet boundary in which reflections have not arrived within the time window of interest. Figure 5(a) shows these two results together, while Fig. 5(b) shows the difference. The PML result and the reference are almost indistinguishable at the signal scale. Compared to incident signal, the reflection is about 50 dB down.

B. Validation of numerical results

An analytical solution for the particle velocity field in a homogeneous, fluid-saturated poroelastic medium subject to a point source in 3-D space or a line source in 2-D space can be derived.⁶ The particle velocity is obtained in a closed form via potential functions.

For Biot's equations, it is convenient to solve for the particle velocity through potential functions. The velocity of particles and body force at source can be expressed in terms of potentials as

$$\mathbf{u} = \nabla \psi_s + \nabla \times \Psi_s,$$

$$\mathbf{U} = \nabla \psi_f + \nabla \times \Psi_f,$$

$$\mathbf{f} = \nabla \Phi + \nabla \times \Psi,$$

where $\nabla \cdot \Psi_f = 0$, $\nabla \cdot \Psi_s = 0$ and $\nabla \cdot \Psi = 0$ and describe the rotational potentials, while ψ_s , ψ_f and Φ describe the dilatational potentials. If the source is purely dilatational, then its rotational component disappears. In the time domain, for a purely P-wave point source and ideal nonviscous fluid, the potential can be expressed as

$$\psi_s(r, t) = \frac{\alpha s(t - r/V_f) + \beta s(t - r/V_s)}{4\pi r},$$

$$\psi_s(r, t) = \frac{\alpha A_f s(t - r/V_f) + \beta A_s s(t - r/V_s)}{4\pi r},$$

where r is the distance and $s(t)$ is the source time function. A_f and A_s represent the ratios between the solid and fluid motion for the fast P wave and the slow P wave. The coefficients α and β are determined by the regularity conditions. V_f and V_s are the velocities of the fast P wave and the slow P wave, respectively.

In two dimensions, for a pure P-wave line source along the y axis, the solution can be obtained by integrating the point source solution in the y direction. In the $x-z$ plane, the dilatational potentials are

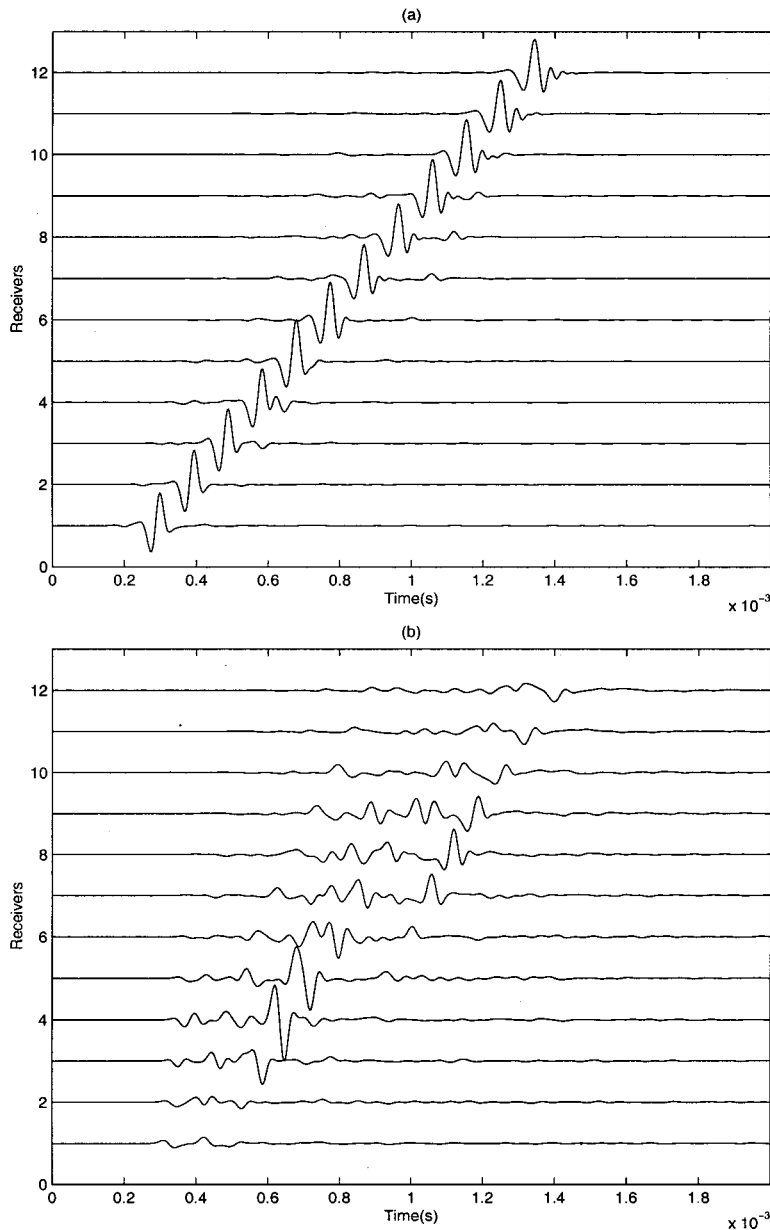


FIG. 8. Seismograms of the vertical particle velocity on the surface for a plastic minelike object in a “dry sand” model. (a) The total field. (b) The scattered field.

$$\begin{aligned} \psi_s(x, z, t) &= \frac{\alpha H(t - r/V_f)}{2\pi} \int_{r/V_f}^t \frac{s(t - \tau)}{\sqrt{\tau^2 - r^2/V_f^2}} d\tau \\ &\quad + \frac{\beta H(t - r/V_s)}{2\pi} \int_{r/V_s}^t \frac{s(t - \tau)}{\sqrt{\tau^2 - r^2/V_s^2}} d\tau, \\ \psi_f(x, z, t) &= \frac{\alpha A_f H(t - r/V_f)}{2\pi} \int_{r/V_f}^t \frac{s(t - \tau)}{\sqrt{\tau^2 - r^2/V_f^2}} d\tau \\ &\quad + \frac{\beta A_s H(t - r/V_s)}{2\pi} \int_{r/V_s}^t \frac{s(t - \tau)}{\sqrt{\tau^2 - r^2/V_s^2}} d\tau, \end{aligned}$$

where $H(\cdot)$ is the Heaviside step function and $r = \sqrt{x^2 + z^2}$. Once the potential functions are available, the velocity can be easily obtained by taking the gradient of potential functions.

The validation of the numerical method can be done by comparing the numerical results with the above analytical

solution. A homogeneous model whose parameters are the same as the previous model is considered. A P-wave line source of the first derivative Gaussian time function with $f_0 = 40$ Hz is located at $(0, 0)$. Then the solution at $(30 \text{ m}, 30 \text{ m})$ is calculated numerically and analytically. The numerical solutions for two different grid spacings are displayed with an analytical solution in Fig. 6. The oscillatory tails and disagreement in Fig. 6(a) for a coarser grid are caused by the dispersion of the slow P wave. When the grid spacing is decreased, the numerical solutions agree well with the analytical solution in Fig. 6(b).

C. Applications

This algorithm can be used to characterize a reservoir in a large scale as well as to investigate soil property in a small scale. In this section, this method is used to model a plastic minelike object that is difficult to detect with the more conventional electromagnetic induction sensors (i.e., metal de-

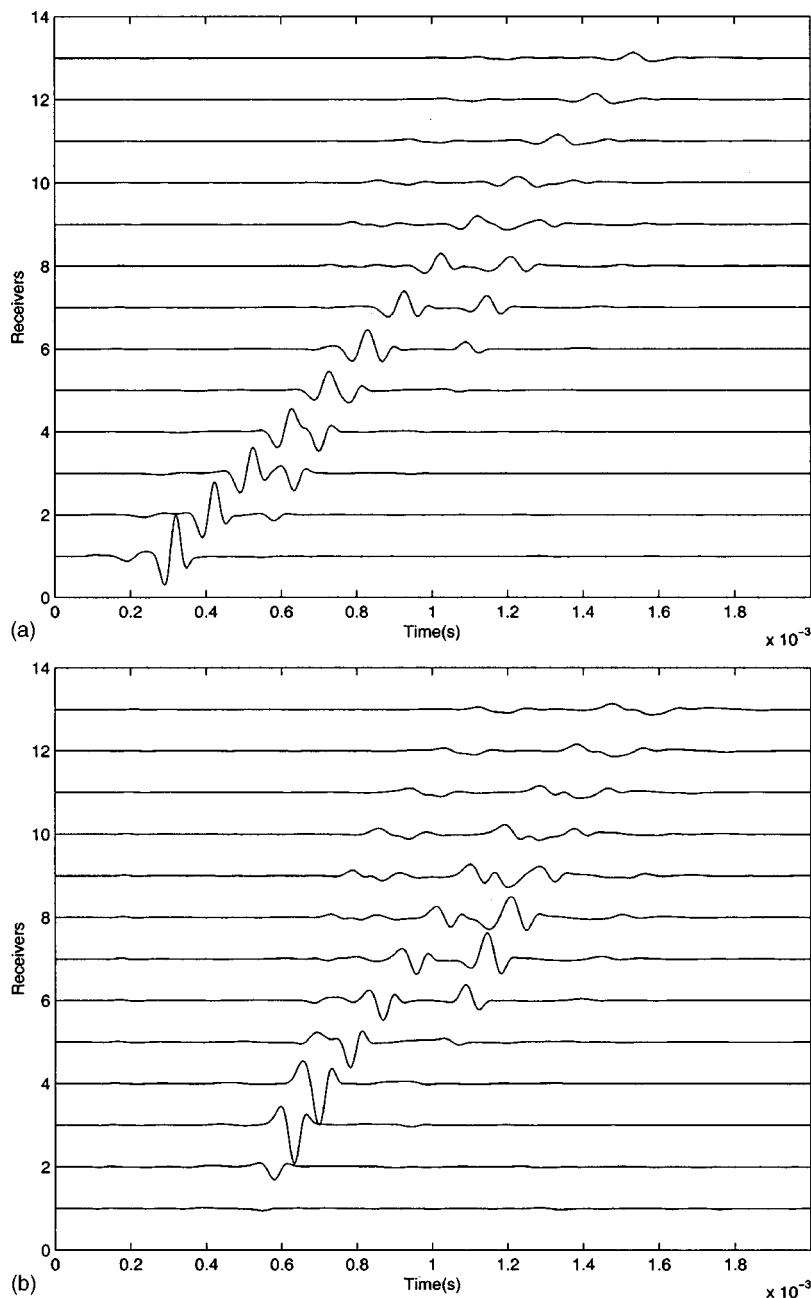


FIG. 9. Same as Fig. 8 except for the “sand” model.

tectors). The geometry of the model of a buried object is shown in Fig. 7.

For the plastic minelike object, the parameters are chosen as $\rho = 1330 \text{ kg/M}^3$, S-wave velocity $v_{\text{shear}} = 417 \text{ m/s}$ and P-wave velocity $v_p = 1060 \text{ m/s}$. The material in the ground may be considered as a two-phase composite material consisting of granular solid and pore fluid. The nature of this composite varies with environment, geographic location, and with depth below the surface of ground. Three different types of soil—dry “sand,” “sand” and “mud”—are used. The first is similar to a coarse sand deposit saturated with air. The second is similar to a coarse sand deposit saturated with water. The third is similar to a fine clay mixture or mud. The elastic properties of these materials are listed next and in Table I.

Grain and fluid properties $K_s = 3.6 \times 10^{10} \text{ Pa}$
 $K_f = 2.0 \times 10^9 \text{ Pa}$

Viscosity $\rho_s = 2650 \text{ kg/m}^3$
 Sound speed of fluid $\rho_f = 1000 \text{ kg/m}^3$
 $\eta = 1.0 \times 10^{-3} \text{ Mks}$
 $C_0 = 1414 \text{ m/s}$

A vertical dipole line source with the first derivative of Gaussian pulse with center frequency of 15 kHz is located on the free surface. The receivers are uniformly distributed on the free surface at a distance 2 to 14.5 cm from the source. The plastic minelike object is buried in the ground with its upper edge 2 cm beneath the surface of the ground. The space step is chosen such that there are 15 grid points per minimum wavelength. The time step is chosen according to the stability condition. Because the minimum wave velocity is different, these three models have a different grid size and number of cells. The computational domain contains 600×160 cells for the “dry sand” model, 400×100 cells for the

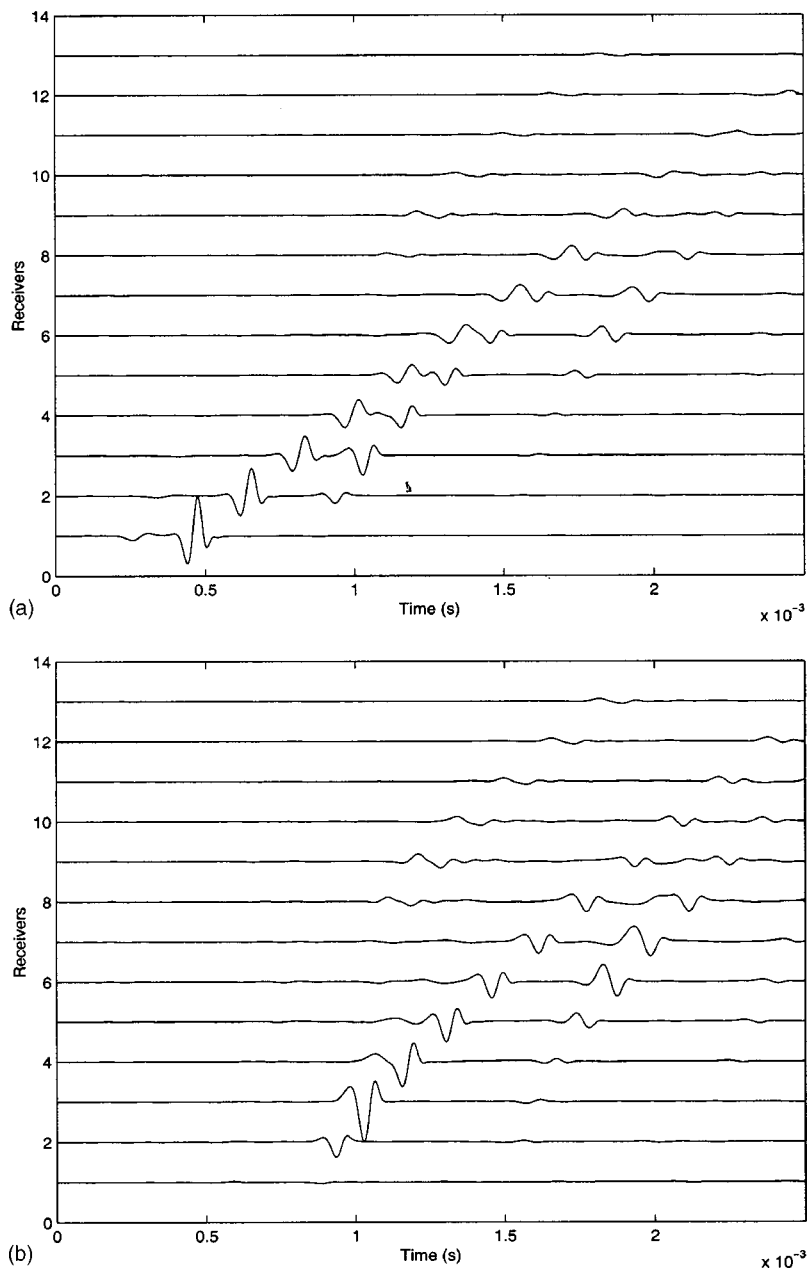


FIG. 10. Same as Fig. 8 except for the “mud” model.

“sand” model, and 600×160 for the “mud” model, including a PML region with a thickness of 10 cells.

The numerical simulations of the soil with plastic mine-like objects were carried out to examine the effects of the plastic object on the wave field and investigate the possibility of the detection of a plastic object in the ground by using acoustic method. Figure 8(a) shows the synthetic seismograms of the vertical velocity of solid particle at the surface for the dry sand model. Here, the vertical velocity is plotted as a function of time and vertically offset by the distance from the source. The wave speed is indicated by the slope of the traveling waves in the figure. Clearly, the Rayleigh surface wave dominates the wave field. In the scattered field in Fig. 8(b) (obtained by subtracting the background field from the total field), the reflected shear wave dominates the wave field. Figures 9(a) and (b) show the total field and scattered field for the “sand” model. In the total field, a strong Ray-

leigh surface which has lower speed than the shear wave is present. The reflected shear wave can be seen clearly just behind the surface wave on the first several traces. Because it has a higher speed, it surpasses the surface wave at far offsets. In this figure, the reflected shear wave dominates other waves. Figures 10(a) and (b) show the total and scattered fields respectively for the “mud” model. The results are very similar to those of the “sand” model except that the speeds of surface waves and shear waves are much lower.

IV. CONCLUSION

A particle velocity-strain, finite-difference method combined with the perfectly matched layer (PML) has been formulated in three dimensions for the simulation of seismic waves propagating in porous media. The performance of the PML boundary in two dimensions has been studied on a

homogeneous model by calculating the reflection from the boundary. The analytical solution to Biot's equations is used to validate the numerical algorithm. The results show that the first-order, leap-frog, staggered-grid scheme has a higher accuracy than the second-order, centered-grid finite-difference scheme. Even with only a 10-cell PML region, the reflection is much less than that of second-order centered-grid scheme with 20-cell PML. The results also show the scheme is stable even if the ratio of the fast P-wave velocity to shear wave velocity is greater than 2.

This numerical method has been used to investigate the interaction of elastic waves with a buried minelike object. Three cases have been investigated: a plastic object buried in purely dry "sand," in "sand," and in "mud." The results show that the wave responses are substantially different for different backgrounds.

- ¹M. A. Biot, "Theory of propagation of elastic waves in a fluid-saturated porous solid. 1. Low-frequency range," *J. Acoust. Soc. Am.* **28**, 168–178 (1956).
- ²M. A. Biot, "Theory of propagation of elastic waves in a fluid-saturated porous solid. 2. Higher-frequency range," *J. Acoust. Soc. Am.* **28**, 179–191 (1956).
- ³M. A. Biot, "Mechanics deformation and acoustic propagation in porous media," *J. Appl. Phys.* **33**, 1482–1498 (1962).
- ⁴S. Hassanzadeh, "Acoustic modeling in fluid saturated porous media," *Geophysics* **56**, 424–435 (1991).
- ⁵X. Zhu and G. A. McMechan, "Finite-difference modeling of the seismic response of fluid saturated, porous, elastic media using Biot theory," *Geophysics* **56**, 328–339 (1991).
- ⁶N. Dai, A. Vafidis, and E. R. Kanasewich, "Wave propagation in heterogeneous, porous media: A velocity-stress, finite-difference method," *Geophysics* **60**, 327–340 (1995).
- ⁷C. Cerjan, D. Kosloff, R. Kosloff, and M. Reshef, "A non-reflecting

- boundary condition for discrete acoustic and elastic wave equations," *Geophysics* **50**, 705–708 (1985).
- ⁸R. Clayton and B. Engquist, "Absorbing boundary conditions for acoustic and elastic wave equations," *Bull. Seismol. Soc. Am.* **67**, 1529–1540 (1977).
- ⁹K. D. Mahrer, "An empirical study of instability and improvement of absorbing boundary conditions for elastic wave equation," *Geophysics* **51**, 1499–1501 (1986).
- ¹⁰J. P. Berenger, "A perfectly matched layer for the absorption of electromagnetic waves," *J. Comput. Phys.* **114**, 185–200 (1994).
- ¹¹W. C. Chew and Q. H. Liu, "Perfectly matched layers for elastodynamics: A new absorbing boundary condition," *J. Comput. Acoust.* **4**, 72–79 (1996).
- ¹²Q. H. Liu, "Perfectly matched layers for elastic waves in cylindrical and spherical coordinates," *J. Acoust. Soc. Am.* **105**, 2075–2084 (1999).
- ¹³F. D. Hastings, J. B. Schneider, and S. L. Broschat, "Application of the perfectly matched layer (PML) absorbing boundary condition to elastic wave propagation," *J. Acoust. Soc. Am.* **100**, 3061–3069 (1996).
- ¹⁴Q. H. Liu and J. Tao, "The perfectly matched layer for acoustic waves in absorptive media," *J. Acoust. Soc. Am.* **102**, 2072–2082 (1997).
- ¹⁵Y. Q. Zeng, J. He, and Q. H. Liu, "The application of the perfectly matched layer in numerical modeling of wave propagation in poroelastic media," Research Report, Duke University (1999).
- ¹⁶R. Burridge and J. B. Keller, "Poroelasticity equations derived from microstructure," *J. Acoust. Soc. Am.* **70**, 1140–1146 (1981).
- ¹⁷J. Plona, "Observation of the second bulk compressional wave in a porous medium at ultrasonic frequencies," *Appl. Phys. Lett.* **36**, 259–261 (1980).
- ¹⁸G. Kneib and C. Kerner, "Accurate and efficient seismic modeling in random media," *Geophysics* **58**, 576–588 (1993).
- ¹⁹Q. H. Liu, F. Daube, C. Randall, E. Schoen, H. Liu, and P. Lee, "A 3D finite difference simulation of sonic logging," *J. Acoust. Soc. Am.* **100**, 72–79 (1996).
- ²⁰Q. H. Liu, "Some current trends in numerical methods for transient acoustic and elastic waves in multidimensional inhomogeneous media," *Current Topics Acoustical Research* **2**, 31–42 (1998).
- ²¹J. I. Dunlop, "Propagation of acoustic waves in marine sediments, a review," *Exploration Geophysics* **19**, 513–535 (1988).